
ONION: Physics-Informed Deep Learning Model for Line Integral Diagnostics Across Fusion Devices

Cong Wang^{1,†}, Weizhe Yang², Haiping Wang¹, Renjie Yang¹, Jing Li¹, Zhijun Wang¹, Xinyao Yu⁴, Yixiong Wei¹, Xianli Huang³, ZhaoYang Liu¹, Changqing Zou¹, Zhifeng Zhao^{1,*}

1 Zhejiang Lab, Hangzhou 310000, China

2 UNSW Sydney, Sydney, NSW, AU

3 ENN Science and Technology Development Co Ltd, Langfang, CN

4 Zhejiang University Hangzhou, Zhejiang, CN

**Corresponding author*

+Contact person

Abstract

This paper introduces a Physics-Informed model architecture that can be adapted to various backbone networks. The model incorporates physical information as additional input and is constrained by a Physics-Informed loss function. Experimental results demonstrate that the additional input of physical information substantially improve the model's ability with a increase in performance observed. Besides, the adoption of the Softplus activation function in the final two fully connected layers significantly enhances model performance. The incorporation of a Physics-Informed loss function has been shown to correct the model's predictions, bringing the back-projections closer to the actual inputs and reducing the errors associated with inversion algorithms. In this work, we have developed a Phantom Data Model to generate customized line integral diagnostic datasets and have also collected SXR diagnostic datasets from EAST and HL-2A. The code, models, and some datasets are publicly available at <https://github.com/calledice/onion>.

Keywords: PINN; Deep learning; Tokamak; EAST; HL-2A; Soft x-rays

1 Introduction

Deep Learning has recently emerged as a pivotal tool in the field of tokamak research, offering a means to expedite computationally intensive tasks and to delve into extensive experimental data sets. Since 2019, there has been a surge in research focusing on the prediction of plasma instabilities using deep learning techniques¹⁻⁴. A novel deep learning approach was introduced for forecasting disruptions in tokamak reactors, showcasing its potential to bolster fusion energy science and the prediction of complex systems⁵. This method provides reliable, high-performance predictions across various machines by leveraging high-dimensional data and supercomputing resources. In recent years, publications in Nature have sparked renewed interest in the application of deep reinforcement learning for plasma control^{6,7}.

In these applications, sensory data from direct measurements can be readily interpreted by Artificial Intelligence (AI) systems and subsequently utilized for event prediction and plasma control. Although AI is often regarded as a "black box" due to its opaque decision-

making processes, it has nonetheless achieved results that surpass those of previous methodologies. However, understanding the underlying changes within the plasma and the reasons behind these outcomes is a matter of keen interest for physicists. Gaining insights into these phenomena is crucial for further comprehension and control of plasma behavior. Moreover, plasma experiments are costly and opportunities to conduct them are scarce, making it imperative to obtain intuitive and rapid physical insights to assist physicists and operators in making decisions between experimental shots. Therefore, the rapid inversion of diagnostic signals to quickly glean information about the plasma's interior is highly necessary. This can provide a basis for shot-to-shot analysis and decision-making. For traditional nuclear fusion diagnostics and inversion, precise physical models are required, which must be based on first principles, taking into account spatial and temporal dynamics, multi-physical fields, and system coupling⁸. This implies that the complexity of the models and the computational time required will significantly increase. A promising approach to address this challenge is the development of AI-based diagnostic inversion surrogate models. The relevant work and its implications will be elaborated in Section 2.

The rapid advancement of artificial intelligence is largely attributed to the global open-source sharing of algorithms, data, and models, which allows researchers to continually build upon the state-of-the-art (SOTA) and push the boundaries of knowledge. The objective of this paper is to construct a highly transferable and robust Physics-Informed model that can be adapted to various backbone networks. Furthermore, the training data and models will be made openly available to the fusion community, thereby fostering the development of a model and data ecosystem within the field of nuclear fusion.

This paper introduces a novel Physics-Informed model grounded in deep learning shown in Figure 1, which leverages natural language processing (NLP) techniques and significantly enhances the capabilities of data-driven methodologies. Physical diagnostic information is integrated into the model through positional encoding, allowing the model to incorporate the physical characteristics of the device and diagnostic systems during the inversion process. Additionally, physical constraints are incorporated into the loss function, which enhances the interpretability of the results and the model's transferability.

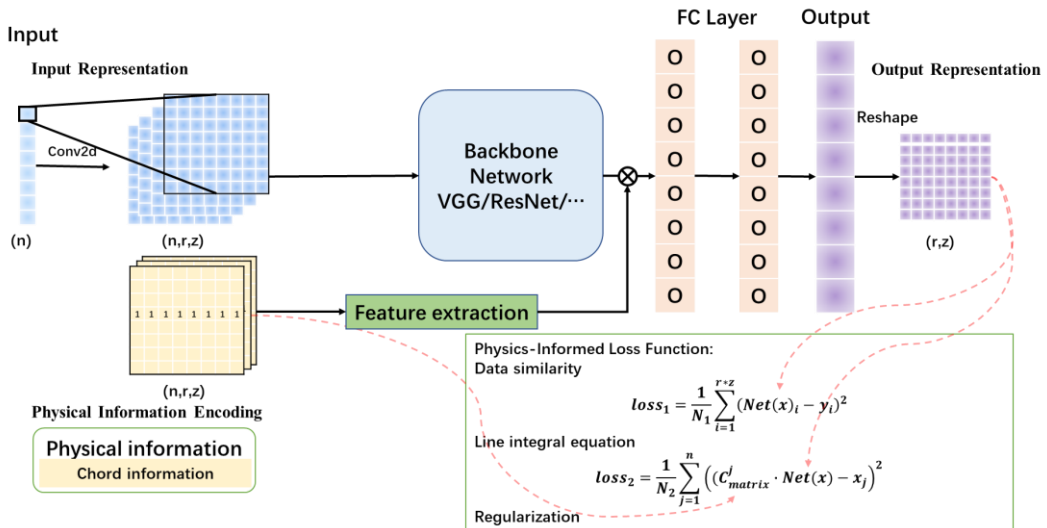


Figure 1 Model structure of Physics-Informed model

The structure of this paper is as follows: Section 2 reviews the advancements in research

on surrogate models for string integral diagnostics in nuclear fusion and analyzes the existing shortcomings. Section 3 presents the four datasets utilized in this study and evaluates the quality of the labels within these datasets. Section 4 details the model architecture, including the input and output representations, the encoding of physical information, the construction of the Physics-Informed loss function, and the backbone network employed. In Section 4, a comparative analysis of the performance of several models is conducted, followed by a discussion. Section 5 concludes the paper and provides an outlook on future work.

2 Related work

Diogo R. Ferreira et al.⁹ use a deconvolutional network that receives the bolometer measurement as input (a total of 56 lines of sight from both cameras) and produces a 120×200 reconstruction of the plasma radiation profile. They also discussed how recurrent neural networks (RNNs) could be used to predict plasma disruptions with sequences of 200 time points of inputs.

In ¹⁰, Marko Blatzheim et al. present the successful reconstruction of proxies for two independent, important edge magnetic field properties given simulated heat load images on the Wendelstein 7-X divertor target plates. The input picture dimensionality is 113×29 and the outputs are two independent, important edge magnetic field properties. Six different artificial neural network architectures from shallow and simple feed-forward fully-connected neural network to deep Inception ResNets with 24223 to 804804 free parameters are investigated.

F. Matos et al.¹¹ uses the Visual Geometry Group Net (VGG-Net)¹² and the Keras framework for deep learning. The network itself receives two inputs: a tomographic projection (208 SXR measurements) and a corresponding mask of ones and zeros which gives information regarding which measurements in the projection are assumed to be faulty. The network outputs are probabilities over 27 possible classes.

Chaowei Mai et al.¹³ builds three typical neural networks, including VGG-Net, a fully affine neural network (FANN) and a fully convolutional neural network (FCNN), to reconstruct a two-dimensional SXR profile. The input SXR data comprise a 92×100 matrix and the 2D SXT label image is the result of linear interpolation on a 75×50 (3750)-dimensional square grid, from the SXR 2D emissivity profile given by the Fourier–Bessel code.

Zhijun Wang et al.¹⁴ build two typical neural networks are carried out and trained, including an up-convolutional neural network and time series neural network to predict the reconstructions of emission profiles for the soft X-ray diagnostics of the HL-2 A tokamak. The input data, consisting of measurements taken from 40 viewing chords, is represented as a 1D vector of length 40, while the target value is a 1D vector of length 1152 derived from the SXR emissivity profiles provided by the NSGPT code.

In summary, modifying the architecture of the main neural network to create distinct surrogate models for line integral diagnostic systems of different devices is often an exercise of limited value. On one hand, such surrogate models tend to have poor transferability, which restricts their application across various setups. On the other hand, with the rapid evolution of neural network models^{15–22} in the fields of natural language processing (NLP) and computer vision (CV), the pursuit of such endeavors can become an endless endeavor, diminishing their overall significance.

In response to these challenges, we have developed a novel Physics-Informed model based on physical information and principles of diagnostic systems. By integrating diagnostic physical information, such as contribution matrices through positional encoding, and the Physics-Informed loss function, our model accounts for the physical characteristics of the device and diagnostic systems. This approach circumvents the limitations of current diagnostic surrogate models, which rely solely on data-to-data mappings without considering the physical context, such as the device and measurement channel positions. These models often suffer from poor transferability, lack of physical interpretability, and are proprietary in nature. Furthermore, our model allows for the flexible selection of advanced backbone neural network structures as its core, ensuring that it can leverage the latest advancements in the field.

3 Dataset

In this work, we have developed a model known as Phantom data Model, designed for the generation of phantom data for line integral diagnostics. This model leverages a forward line integral model to create simple 2D physical fields (labels) of arbitrary region sizes and their corresponding exact line integral results (inputs), free from algorithm errors including systematic error and random error. Additionally, we have compiled datasets from line integral diagnostic measurements obtained from two tokamak facilities: EAST and HL-2A.

The phantom dataset for line integrals is generated using the Phantom data Model, which allows for parameter customization based on the characteristics of the actual line integral diagnostic inversion results from tokamak devices. Parameters such as the number of radial grid points ($numr$), the number of vertical grid points ($numz$), and the contribution matrix (C_{matrix}) can be set accordingly. The model randomly selects a central point within the grid area and initializes it with a maximum value. Subsequently, it assigns values to each grid point based on the positional relationship with the central point and the given assignment rules, thus obtaining a complete 2D physical field. By applying the principles of line integration and multiplying the contribution matrix with the label, the model generates a line integral result (input) that is strictly free from algorithm errors. The flowchart of the Phantom data Model and the examples of the generated outputs are illustrated in the Figure 2.

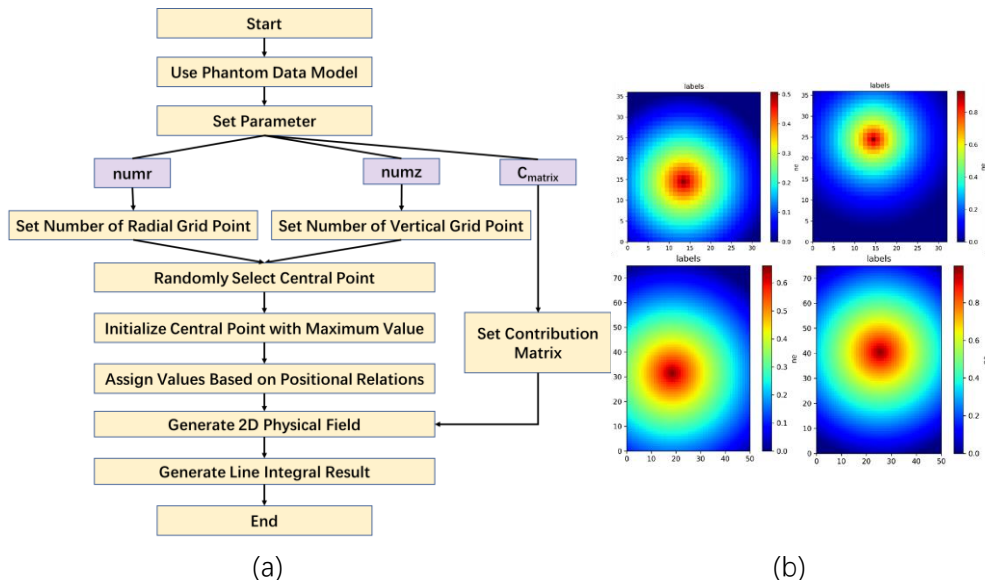


Figure 2: (a) The flowchart of the Phantom data Model; (b) The examples of the generated outputs.

The dataset from EAST is built by Chaowei Mai ¹³. Figure 3 (a) provides an overview of the basic information regarding the Soft X-ray (SXR) diagnostics. The cameras are equipped with 46 detectors each for the Upper (U) and Lower (D) arrays, and 30 detectors for the Vertical (V) array, all capable of delivering independent SXR measurements. The raw data extracted from the EAST SXR cameras, specifically U and D, serve as inputs (92) to our model. The corresponding labels (75×50) are generated from 2D Soft X-ray Tomography (SXT) images, which are produced using Fourier-Bessel SXT codes.

The dataset from HL-2A is constructed by Zhijun Wang ¹⁴. The experimental configuration of the Soft X-ray (SXR) diagnostic for HL-2A is depicted in Figure 3 (b). A total of 40 viewing chords from Cameras No. 3 and No. 4 were utilized as inputs, with each camera being equipped with 20 Si-PIN photon-diode detectors. The label consists of a 36×32 grid, representing a 2D profile image that is derived from the SXR emissivity profiles calculated by the NSGPT code ²³.

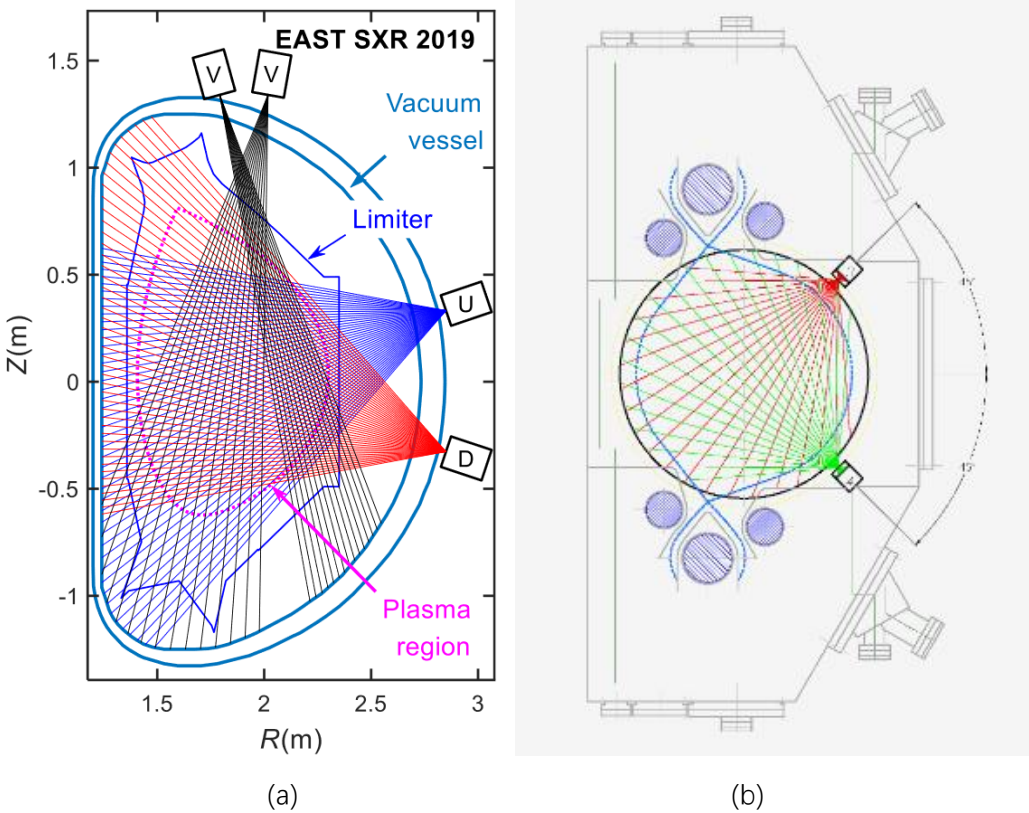


Figure 3: (a) EAST cross section and three cameras (U, D and V) of the SXR diagnostic with locations of their LOSs shown (three piles of lines); (b) The experimental configuration of the Soft X-ray (SXR) diagnostic for HL-2A.

The principle of the line integral diagnostic is encapsulated in Equation (3-1), where x_i represents the measurement value of the i -th chord. R denotes the forward process that transforms the 2D emission into line-integrated data, calculated by considering the starting and ending positions, as well as the beam width of the lines-of-sight (LOS). The term Δ_i accounts for the systematic and statistical errors encountered in actual experiments. The contribution matrix for the i -th chord is denoted by C_{matrix}^i , and y^j is the label corresponding to the j -th sample. The quality of the j -th sample can be assessed using Mean

Relative Error (MRE) ε_j of back-projections (BPs)¹¹ for the physical validation, as shown in Equation (3-2). Hence, the quality of the dataset can be assessed by $\bar{\varepsilon}$, as shown in Equation (3-3), where $\bar{\varepsilon}$ also indicates the goodness of various inversion algorithms. Figure 4 presents the ε_j of a single sample across different datasets. The $\bar{\varepsilon}$ of Phantom_East and Phantom_HL-2A are close to 0, which means the data rigorously adheres to the principles of physical line integration. The $\bar{\varepsilon}$ of Exp_East and Exp_HL-2A are $4.96E^{-2}$ and $5.42E^{-2}$, respectively. Table 1 presents an overview of the basic information for each dataset.

$$x_i = R_i(y) + \Delta_i = C_{matrix}^i \cdot y + \Delta_i \quad 3-1$$

$$\varepsilon_j = \frac{1}{n} \sum_{i=1}^n \left| \frac{x_i^j - C_{matrix}^i \cdot y^j}{x_{max}^j} \right| \quad 3-2$$

$$\bar{\varepsilon} = \frac{1}{m} \sum_{j=1}^m (\varepsilon_j) \quad 3-3$$

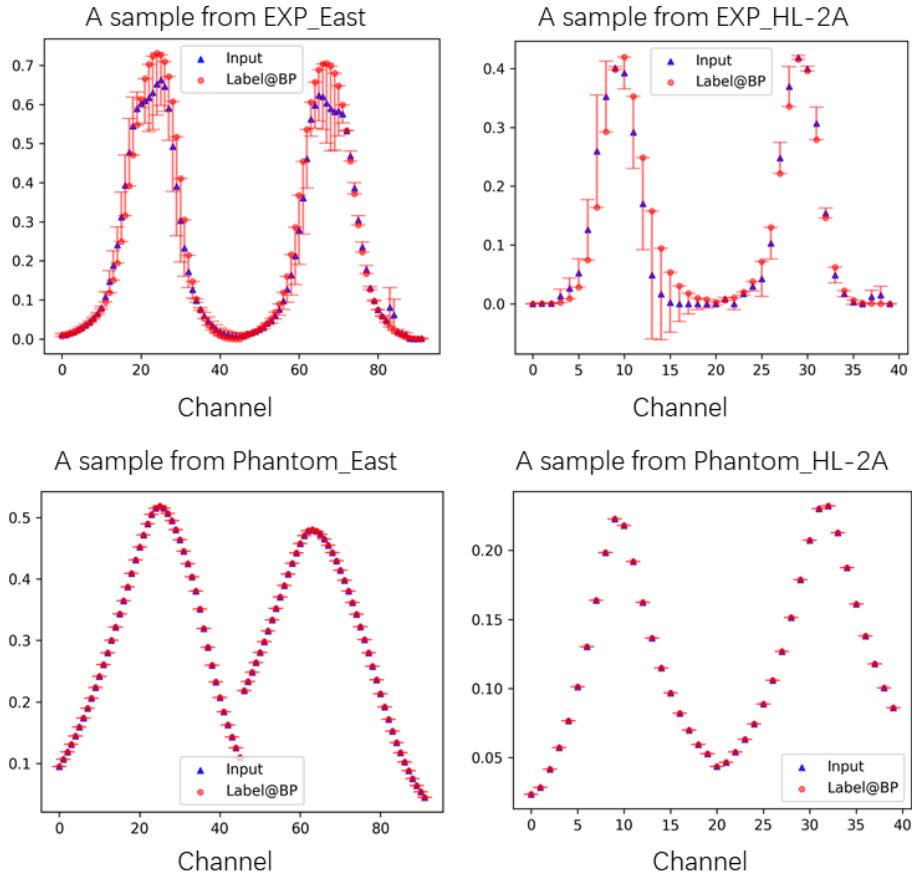


Figure 4 ε_j of back-projections (BPs) across different datasets.

Table 1 An overview of the basic information for datasets.

Dataset	Input_size	Label_size	Train_Num	Valid_Num	Test_Num	Error ($\bar{\varepsilon}$)
Phantom_East	92	75*50	70000	19999	10001	$3.70E^{-8}$
Phantom_HL-2A	40	32*36	70000	19999	10001	$2.54E^{-8}$
Exp_East	92	75*50	30364	8676	4338	$4.96E^{-2}$
Exp_HL-2A	40	32*36	459120	153040	153040	$5.42E^{-2}$

4 Model Architecture

The goal of this project is to enhance the performance of the backbone neural network by developing a Physics-Informed model, which aims to optimize the construction of surrogate models for line integral diagnostic systems. The model utilizes n measurement signals from the diagnostic system as input and the outcomes of inversion algorithms as labels. Our training process incorporates four datasets: two are synthetically generated using a phantom data model, while the other two are obtained from experimental data of the EAST and HL-2A.

Model Design and Training Details: Our Physics-Informed model is meticulously designed with several key components: an input representation layer to transfer input information to higher dimensions for better feature extraction and easy merging with physical information; a physical information feature extraction side chain to extract diagnostic physical information, and feed it into the following neural network; a backbone network layer that offers the flexibility to select a high-performance neural network structure as the core; and an output representation layer, which consists of two fully connected layers for final output computation. We employ the Adam optimizer with an initial learning rate of 0.0001. To further refine the training process, we have implemented a cosine annealing strategy to adjust the learning rate cyclically. This strategy operates over a period of 50 epochs, during which the learning rate is gradually reduced to a minimum value of 0.00001. The cosine annealing method is particularly effective in managing the convergence rate, as it helps to avoid potential stalls in training progress that can occur with static or prematurely reduced learning rates. The loss function is a combination of Mean Square Error (MSE), a physical constraint loss derived from the principles of line integration, and an L2 regularization term to assess the model's predictive accuracy. The training process is executed on an NVIDIA V100 GPU, encompassing a total of 50 epochs. To prevent overfitting and to optimize training efficiency, an early stopping strategy has been implemented. This strategy is triggered if there is no improvement in the validation losses for 25 consecutive epochs. The hyperparameters are set with a batch size of 256 and a weight decay (L2 regularization) coefficient of 0.0001.

4.1 Input and Output Representation

Before entering the backbone network, the input data undergoes a transformation by a 2D convolutional layer, converting one-dimensional data into two-dimensional representations ((n) to (n, z, r)). This design serves dual purposes: it aligns with the input shape requirements of the main network and enhances the feature representation capabilities of the input data. This conversion enables the model to capture the local correlations and spatial structures present in the input data more effectively. The output from the backbone network is initially flattened to integrate all local features into a single global feature vector. Subsequently, this vector is processed through fully connected layers, which facilitates the learning of global relationships among the features. For the final fully connected layer, either ReLU or Softplus activation functions are employed.

4.2 Physical Information Encoding

As depicted in Figure 1, the encoding diagram is inspired by the work of Tailin Wu ²⁴. The physical information of the device primarily consists of chord information. Chord information refers to the contribution matrix data of the chords within the diagnostic system. Each chord's contribution matrix is represented as an $r * z$ matrix for a single channel, with n chords corresponding to n channels. Figure 5 displays the grayscale images of the contribution matrices for several channels of the EAST device, as well as the grayscale image obtained by summing the contribution matrices of all 92 channels. Figure 6 presents the grayscale images of the contribution matrices for several channels of the HL-2A device, the grayscale image derived from the sum of the 40 channels' contribution matrices. The encoded physical information (n, z, r) is fed into the feature extraction side chain as shown in Table 2. The feature extraction side chain is a streamlined version of the VGG model architecture. The extracted features are then integrated with the output of backbone network through a multiplication process, facilitating the fusion of information in a manner that enhances the model's predictive capabilities.

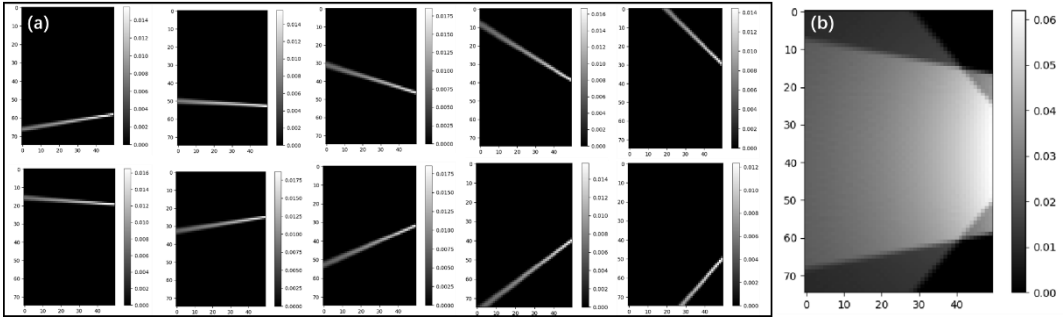


Figure 5: (a) The grayscale images of contribution matrices for several channels of the EAST device; (b) The grayscale image obtained by summing the contribution matrices of all 92 channels.

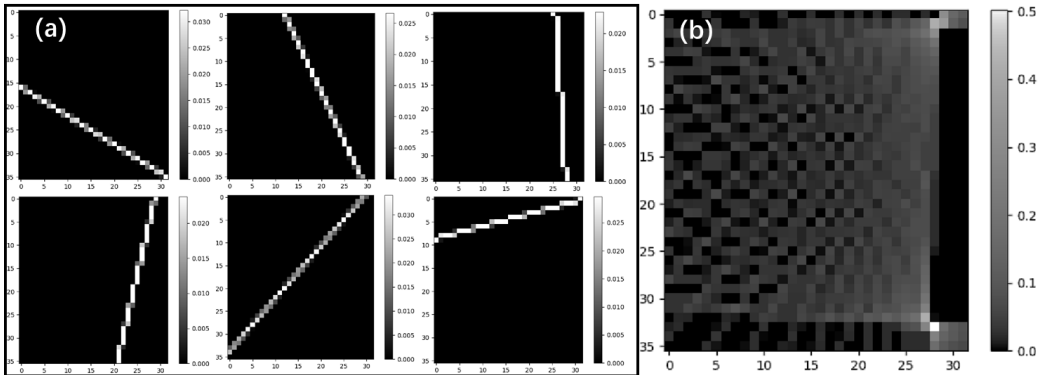


Figure 6: (a) The grayscale images of contribution matrices for several channels of the HL-2A device; (b) The grayscale image obtained by summing the contribution matrices of all 40 channels.

Table 2 Detailed information about the feature extraction side chain.

Physical information(n, z, r)
Conv1 $\begin{bmatrix} 3 \times 3, 2n \\ 3 \times 3, 2n \end{bmatrix} \times 1$
MaxPool2d (2×2)

Conv2 $[3 \times 3, 4n] \times 1$
MaxPool2d (2×2)
Conv3 $[3 \times 3, 8n] \times 1$
AdaptiveMaxPool2d (3×3)
PI($8n, 3, 3$)

4.3 Physics-Informed Loss Function

The Physics-Informed loss function is composed of three distinct components, each serving a specific purpose in the model's training process. Firstly, the discrepancy between the model's predictive outputs and the ground truth labels quantifies the accuracy of the model's predictions. Secondly, the loss function includes the error between the results obtained by forward calculation from the predictive values and the actual inputs, ensuring that the model's internal physics are consistent with the inputs. Lastly, an L2 regularization term is introduced to prevent overfitting by penalizing excessive complexity in the model's parameters. These components are collectively defined in Equation (4-1). We introduce simple weighting coefficients, denoted as w_1 and w_2 for the first two components of the loss function. This design enables the loss function to dynamically adjust the weighting contributions of $loss_2$ based on their relative magnitudes at any given time. The coefficient for the L2 regularization term is set to 0.0001. By doing so, the model training process can adaptively emphasize the components that require more refinement, ensuring a more effective optimization trajectory.

$$L = w_1 \cdot loss_1 + w_2 \cdot loss_2 + \lambda \|w\|_2^2 \quad 4-1$$

$$w_1 = 1.0, loss_1 = \frac{1}{N_1} \sum_{i=1}^{r \times z} (\mathbf{Net}(\mathbf{x})_i - \mathbf{y}_i)^2 \quad 4-2$$

$$w_2 = c_1 \frac{loss_1}{loss_2}, loss_2 = \frac{1}{N_2} \sum_{j=1}^n ((\mathbf{C}_{matrix}^j \cdot \mathbf{Net}(\mathbf{x}) - \mathbf{x}_j)^2 \quad 4-3$$

4.4 Backbone network

The choice of backbone network is arbitrary and can range from established architectures such as VGG¹², ResNet²⁵, Transformer²², Vision Transformer (ViT)¹⁵. In this work, we have constructed two backbone networks, VggOnion and ResOnion, based on VGG and ResNet architectures, respectively. The VggOnion network is composed of 10 hidden layers, including 8 convolutional layers and 2 fully connected layers, featuring a very simple structure with uniformly sized convolution kernels (3×3) and max-pooling dimensions (2×2) throughout the network. The ResOnion network incorporates 18 hidden layers, consisting of 5 residual blocks, 3 down-sampling residual blocks, and 2 fully connected layers.

We have further differentiated the models based on the inclusion of physical information, resulting in four variants: VggOnion, VggOnion-PI, ResOnion, and ResOnion-PI. Models without physical information (PI) input have an input dimension of (n, z, r) . Models equipped

with physical information input incorporate a feature extraction side chain, which is designed to distill pertinent characteristics from the input data. Detailed information about the models is presented in the accompanying Table 3, which concludes with a summary of the model parameters trained on different datasets.

Table 3 Detailed information about the 4 models.

VggOnion	VggOnion-PI	ResOnion	ResOnion-PI
10 weight layers	10 weight layers	18 weight layers	18 weight layers
Input(n,z,r)	Input(n,z,r)	Input(n,z,r)	Input(n,z,r)
Backbone network Configuration			
Conv1 $\begin{bmatrix} 3 \times 3, 2n \\ 3 \times 3, 2n \end{bmatrix} \times 2$		Res1 $\begin{bmatrix} 3 \times 3, n \\ 3 \times 3, n \end{bmatrix} \times 2$	
MaxPool2d (2 \times 2)		Res2_scale $\begin{bmatrix} 3 \times 3, 2n \\ 3 \times 3, 2n \end{bmatrix} \times 1$	
Conv2 $\begin{bmatrix} 3 \times 3, 4n \\ 3 \times 3, 4n \end{bmatrix} \times 3$		Res2 $\begin{bmatrix} 3 \times 3, 2n \\ 3 \times 3, 2n \end{bmatrix} \times 1$	
MaxPool2d (2 \times 2)		Res3_scale $\begin{bmatrix} 3 \times 3, 4n \\ 3 \times 3, 4n \end{bmatrix} \times 1$	
Conv3 $\begin{bmatrix} 3 \times 3, 8n \\ 3 \times 3, 8n \end{bmatrix} \times 3$		Res3 $\begin{bmatrix} 3 \times 3, 4n \\ 3 \times 3, 4n \end{bmatrix} \times 1$	
AdaptiveMaxPool2d (3 \times 3)		Res4_scale $\begin{bmatrix} 3 \times 3, 8n \\ 3 \times 3, 8n \end{bmatrix} \times 1$	
		Res4 $\begin{bmatrix} 3 \times 3, 8n \\ 3 \times 3, 8n \end{bmatrix} \times 1$	
		/	AdaptiveMaxPool2d (3 \times 3)
/	\otimes PI(8n, 3,3)	/	\otimes PI(8n, 3,3)
FC-z * r		FC-z * r	
FC-z * r		FC-z * r	
Total Parameters			
HL-2A: 7,620,672 EAST: 54,620,796	HL-2A: 9,438,432 EAST: 64,226,700	HL-2A: 13,071,792 EAST: 230,353,860	HL-2A: 10,834,512 EAST: 71,599,764

5 Results

This section focuses on the rationale behind the adoption of the incorporation of physical information (PI), the Softplus activation function, and the introduction of additional loss terms. We employ two metrics to evaluate the performance of our models. The first metric is the average relative error between the model's predictions and the labels, denoted as E_1 . The second metric is the average relative error between the back-projections (BPs)¹¹ and the input data, denoted as E_2 . E_1 characterizes the model's fitting capability to the label data; a lower E_1 signifies that the model is more aligned with the inversion algorithms used to generate the labels. E_2 represents the degree to which the model's results conform to physical

principles; a lower E_2 indicates that the model's predictions are more consistent with the underlying laws of physics.

$$E_1 = \frac{1}{m} \sum_{j=1}^m \left(\frac{1}{r * z} \sum_{i=1}^{r * z} \left| \frac{\text{Net}(x^j)_i - y_i^j}{y_{\max}^j} \right| \right) \quad 5-1$$

$$E_2 = \frac{1}{m} \sum_{j=1}^m \left(\frac{1}{n} \sum_{i=1}^n \left| \frac{x_i^j - C_{\text{matrix}}^i \cdot y^j}{x_{\max}^j} \right| \right) \quad 5-2$$

Correspondingly, we use ϵ_1 and ϵ_2 to evaluate the performance of the model on the single test sample.

$$\epsilon_1 = \left| \frac{\text{Net}(x^j)_i - y_i^j}{y_{\max}^j} \right| \quad 5-3$$

$$\epsilon_2 = \left| \frac{x_i^j - C_{\text{matrix}}^i \cdot y^j}{x_{\max}^j} \right| \quad 5-4$$

5.1 Role of Physical Information

In this section, we **use ReLU activation functions** exclusively in the final two fully connected layers of our model to study the impact of integrating **physical information (PI)** on performance. Accordingly, we compare the performance of the VggOnion and VggOnion_PI models, as well as the ResOnion and ResOnion_PI models. This comparative analysis is designed to elucidate the specific contributions of PI to the predictive accuracy and the adherence to physical principles within our models. The models' loss function is solely composed of the term loss_1 .

Because PI is the same for the same tokamak device, it is extremely easy for the neural network model to learn PI as a constant and thus does not directly affect the update of the weights. Here we will use theoretical derivation to explain why we design the side chain structure in this way to allow PI to also participate in the gradient update of the model weight. For a simple network $N(\cdot)$, x is the dynamic input and x' is the PI (static input). If the two are added or concatenated into the model, the output is shown in the Equation (5-5) and Equation (5-6). The weight update of the neuron is only related to the first term in the equations. We tried these ways and the model performed poorly as expected. However, if the two are input into the model by element-wise multiplication, the final result is shown in the Equation (5-7). The neuron weight update will take into account both x and x' . The performance of models using this way is shown in the following Table 4.

$$N(x + x') = \omega x + \omega x' + b \quad 5-5$$

$$N([x, x']) = \omega x + \omega' x' + b \quad 5-6$$

$$N(x * x') = \omega x * x' + b \quad 5-7$$

Table 4 The impact of integrating physical information (PI) on model performance.

Dataset	Phantom_East ($\bar{\epsilon} = 3.70E^{-8}$)					Phantom_HL-2A ($\bar{\epsilon} = 2.54E^{-8}$)			
	Model	VggOnion	VggOnion_PI	ResOnion	ResOnion_PI	VggOnion	VggOnion_PI	ResOnion	ResOnion_PI
E_1		1.02E ⁻²	0.36E⁻²	2.63E ⁻²	0.52E⁻²	0.91E ⁻²	0.53E⁻²	0.95E ⁻²	0.75E⁻²

E_2	1.81E ⁻²	0.56E⁻²	4.88E ⁻²	0.83E⁻²	1.36E ⁻²	0.70E⁻²	1.35E ⁻²	1.03E⁻²
Dataset	Exp_East ($\bar{\epsilon} = 4.96E^{-2}$)				Exp_HL-2A ($\bar{\epsilon} = 5.42E^{-2}$)			
Model	VggOnion	VggOnion_PI	ResOnion	ResOnion_PI	VggOnion	VggOnion_PI	ResOnion	ResOnion_PI
E_1	0.60E ⁻²	0.57E⁻²	0.65E ⁻²	0.57E⁻²	0.37E ⁻²	0.26E⁻²	0.32E ⁻²	0.28E⁻²
E_2	4.95E ⁻²	4.76E⁻²	4.90E ⁻²	4.67E⁻²	5.43E ⁻²	5.42E⁻²	5.46E ⁻²	5.42E⁻²

For datasets with almost zero error $\bar{\epsilon}$ (Phantom_East and Phantom_HL-2A), the introduction of PI has a significant improvement on different models. Both E_1 and E_2 drop significantly, with E_1 dropping by about **52% on average** and E_2 dropping by about **56% on average**. Figure 7 shows the test results of different models on the j th sample in the Phantom_HL-2A test set. With the introduction of PI, the relative error distribution ϵ_1 between the model prediction result and the label is significantly reduced, and according to the relative error distribution ϵ_2 , the back-projection (BP) value (green dot) of the prediction result is closer to the input value (blue triangle).

For datasets from experiments with error $\bar{\epsilon}$ (EXP_East and EXP_HL-2A), VggOnion and ResOnion have demonstrated commendable performance. Consequently, the introduction of PI has a little improvement on different models. E_1 decreased slightly, with **an average decrease of about 15%**, and E_2 **remained almost unchanged**. Figure 8 shows the test results of different models on the j th sample in the EXP_HL-2A test set. The performance of the four models is comparable. By comparing the results from the Phantom datasets with those from the EXP datasets, we can deduce that the noise introduced by data errors ($\bar{\epsilon}$) may restrict the performance improvements that can be achieved by incorporating PI.

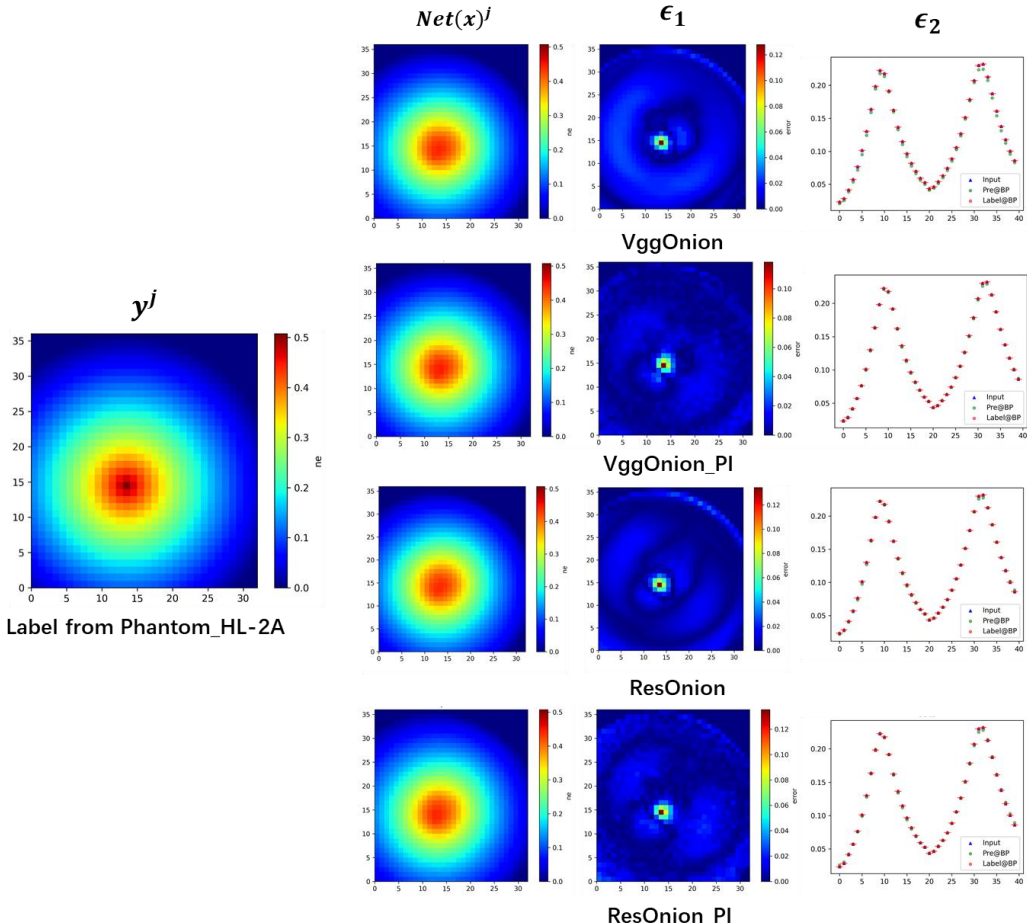


Figure 7 Test results of different models on the j th sample in the Phantom_HL-2A test set.

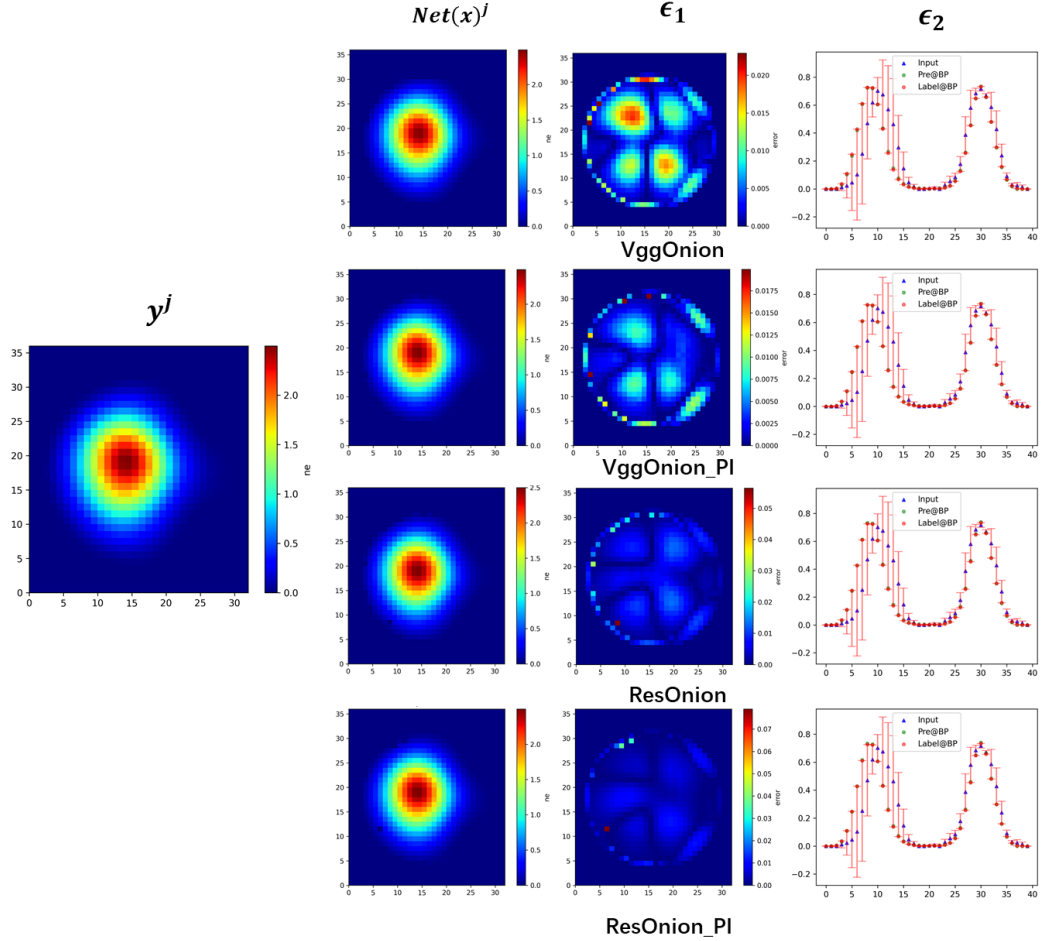


Figure 8 Test results of different models on the j th sample in the EXP_HL-2A test set.

5.2 Role of the Softplus Activation Function

In the results presented in the previous section, we observed significant implausible values at the edges of the predicted result contour plots, i.e., the edges are not smooth. This section primarily focuses on addressing this issue. We think it comes from the characteristics of the ReLU activation function, which is defined as $\max(0, x)$. For $x < 0$, the derivative of the ReLU function drops to zero abruptly. After comparing several activation functions, we find the Softplus function which can be considered a smoothed version of the ReLU function. For $x < 0$, the derivative of the Softplus function gradually decreases, approaching zero. This characteristic helps to mitigate the issue of vanishing gradients that can occur with ReLU when $x < 0$, as it prevents the output from becoming zero and thus maintains a more stable gradient flow during training. The comparative curves of the two activation functions are depicted in Figure 9.

We conduct a comparative analysis between the VggOnion and ResOnion models to evaluate the impact of **activation functions** used in the final two fully connected (FC) layers on model performance. The models' loss function is solely composed of the term $loss_1$. The performance of models with **ReLU or Softplus function** is shown in the following Table 5.

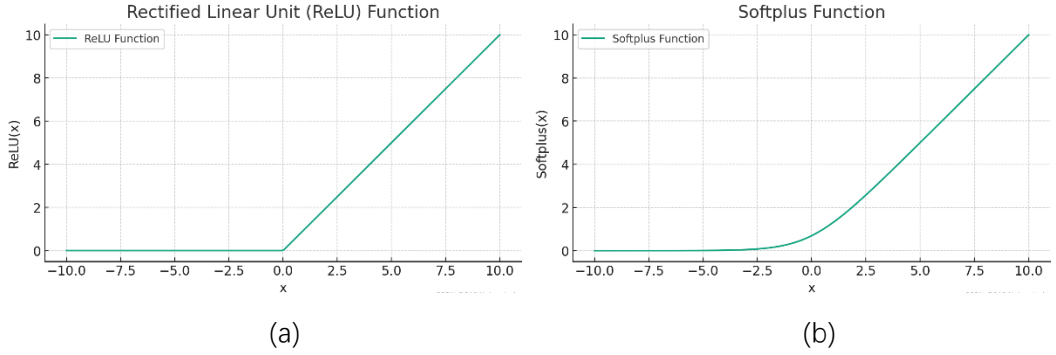


Figure 9: (a) ReLU function; (b) Softplus function.

Table 5 The impact of the Softplus activation function on model performance.

Dataset	Phantom_East ($\bar{\epsilon} = 3.70E^{-8}$)				Phantom_HL-2A ($\bar{\epsilon} = 2.54E^{-8}$)			
Model	VggOnion		ResOnion		VggOnion		ResOnion	
Activation Function	ReLU	Softplus	ReLU	Softplus	ReLU	Softplus	ReLU	Softplus
E_1	1.02E ⁻²	0.27E⁻²	2.63E ⁻²	0.25E⁻²	0.91E ⁻²	0.39E⁻²	0.95E ⁻²	0.36E⁻²
E_2	1.81E ⁻²	0.41E⁻²	4.88E ⁻²	0.44E⁻²	1.36E ⁻²	0.55E⁻²	1.35E ⁻²	0.50E⁻²
Dataset	Exp_East ($\bar{\epsilon} = 4.96E^{-2}$)				Exp_HL-2A ($\bar{\epsilon} = 5.42E^{-2}$)			
Model	VggOnion		ResOnion		VggOnion		ResOnion	
Activation Function	ReLU	Softplus	ReLU	Softplus	ReLU	Softplus	ReLU	Softplus
E_1	0.60E ⁻²	0.51E⁻²	0.65E ⁻²	0.59E⁻²	0.37E ⁻²	0.20E⁻²	0.32E ⁻²	0.20E⁻²
E_2	4.95E ⁻²	4.82E⁻²	4.90E ⁻²	4.69E⁻²	5.43E ⁻²	5.37E⁻²	5.46E ⁻²	5.39E⁻²

Figure 10 compares the performance of the VggOnion and ResOnion models when the activation functions of the final two fully connected (FC) layers are set to ReLU and Softplus, respectively. Upon examining the magnified portions of the figures, it is evident that the results obtained with the Softplus activation function exhibit smoother edges and are more closely aligned with the ground truth labels. This enhanced performance is attributed to the continuous nature of the Softplus function for $x < 0$ and its property of yielding positive output values, which aligns more closely with the characteristics of the underlying physical quantities.

Table 5 reveals that the adoption of the Softplus function also leads to an enhancement in model performance. For Phantom_East and Phantom_HL-2A datasets, the introduction of PI has a significant improvement on two models. Both E_1 and E_2 drop significantly, with E_1 dropping by about **71% on average** and E_2 dropping by about **73% on average**. For EXP_East and EXP_HL-2A datasets, both E_1 and E_2 have decreased slightly, with E_1 decreasing by about **27% on average** and E_2 decreasing by about **2.3% on average**. Once again, a comparison between the Phantom and EXP datasets suggests that the noise resulting from data errors ($\bar{\epsilon}$) may also impede the performance enhancements that could be realized by adopting the Softplus activation function.

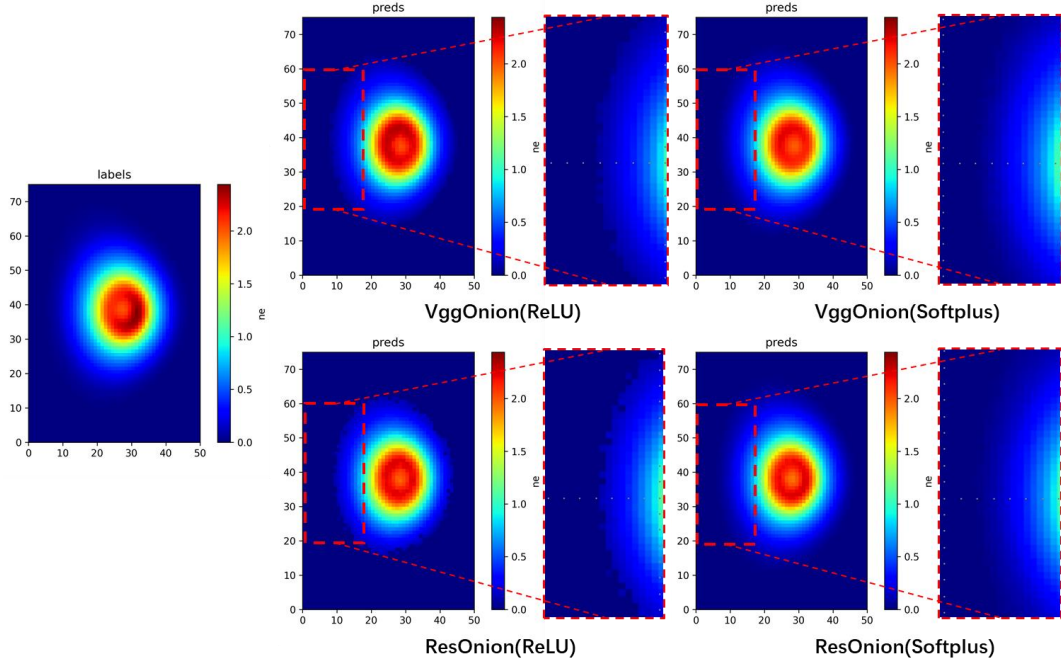


Figure 10 Test results of different models on the j th sample in the EXP_EAST test set.

5.3 Role of the Physics-Informed Loss Function

Building upon the findings from the previous section, this section is dedicated to assessing the impact of the **Physics-Informed loss function (PILF)** on model performance. The models utilized in this section are the **VggOnion_PI** and **ResOnion_PI**. **Softplus function is used** in the final two fully connected (FC) layers. The additional loss terms in the Physics-Informed loss function (PILF) are designed to further refine the model's predictions, ensuring that they not only fit the label data but also satisfy inherent physical constraints.

For the error-free Phantom dataset, closer model predictions to the ground truth labels imply that the back-projection (BP) will also be closer to the input data. In such cases, utilizing the term $loss_1$ is sufficient. However, **for experimental datasets with inherent errors, a close match between model predictions and labels does not guarantee the closeness of the BP to the input.** It is well understood that when BP closely aligns with the input, it indicates that the predictions better satisfy the inherent physical constraints. This alignment, in turn, may lead to a deviation between model predictions and labels for experimental datasets with inherent errors. Therefore, PILF is employed to achieve a balanced optimization. Consequently, this section **adopts experimental datasets** for model training to account for these complexities. **Only E_2** is considered to assess the model. The hyperparameter c_1 of the $loss_2$ must be adjusted according to the model and the dataset to reflect the desired emphasis on inherent physical constraints during model training.

Table 6 presents the performance of the VggOnion_PI and ResOnion_PI models on the Exp_East and Exp_HL-2A datasets. For the Exp_East dataset, the hyperparameter c_1 of the loss function $loss_2$ is set to 0.618, while for the Exp_HL-2A dataset, it is set to 1.0. When compared to the models trained with only $loss_1$, the introduction of the Physics-Informed loss function (PILF) resulted in a decrease in E_2 for different models, with the extent of this reduction being related to the hyperparameter c_1 . This indicates that PILF can effectively

enhance the models' ability to adhere to the inherent physical constraints in their predictions.

Table 6 The impact of the PILF on model performance.

Dataset	Exp_East ($\bar{\epsilon} = 4.96E^{-2}$)				Exp_HL-2A ($\bar{\epsilon} = 5.42E^{-2}$)			
Model	VggOnion_PI		ResOnion_PI		VggOnion_PI		ResOnion_PI	
Loss Function	$loss_1$	PILF $c_1 = 0.618$	$loss_1$	PILF $c_1 = 0.618$	$loss_1$	PILF $c_1 = 1.0$	$loss_1$	PILF $c_1 = 1.0$
E_1	$0.50E^{-2}$	$1.35E^{-2}$	$0.45E^{-2}$	$1.37E^{-2}$	$0.21E^{-2}$	$1.94E^{-2}$	$0.21E^{-2}$	$1.93E^{-2}$
E_2	$5.08E^{-2}$	$4.42E^{-2}$	$4.69E^{-2}$	$3.46E^{-2}$	$5.38E^{-2}$	$0.76E^{-2}$	$5.37E^{-2}$	$0.82E^{-2}$

Figure 11 illustrates the performance of the model on the Exp_East test dataset. Models trained solely with $loss_1$ exhibit a good match between predicted and labeled data, as well as between the back-projections (BP) of the predictions and the labels (red and green dots in ϵ_2), although there is still a discrepancy with the actual input. Models incorporating the Physics-Informed loss function (PILF) show a trend where the BP of the predictions (green dots) deviate from the labeled BP (red dots) and move closer to the input (blue triangles). Due to the hyperparameter c_1 of the loss function $loss_2$ being set to 0.618, the predictions do not align perfectly with the input. The $Net(x)^j$ plot reveals that the models with PILF exhibit a noticeable divergence from the labels in the plasma core region, which is an adjustment introduced by PILF.

Figure 12 demonstrates the performance of the model on the Exp_HL-2A test dataset. Models that incorporate the Physics-Informed loss function (PILF) exhibit back-projections of predictions (green dots) that are nearly indistinguishable from the input (blue triangles). This near-perfect alignment is attributed to the hyperparameter c_1 of the loss function $loss_2$ being set to 1.0, which ensures that the predictions closely match the input. However, this approach also introduces certain issues; for instance, the $Net(x)^j$ plot becomes less smooth. Furthermore, predictions from models utilizing PILF exhibit localized discontinuities at the edges. To mitigate this phenomenon, additional edge regularization terms could be incorporated into the loss function in future work.

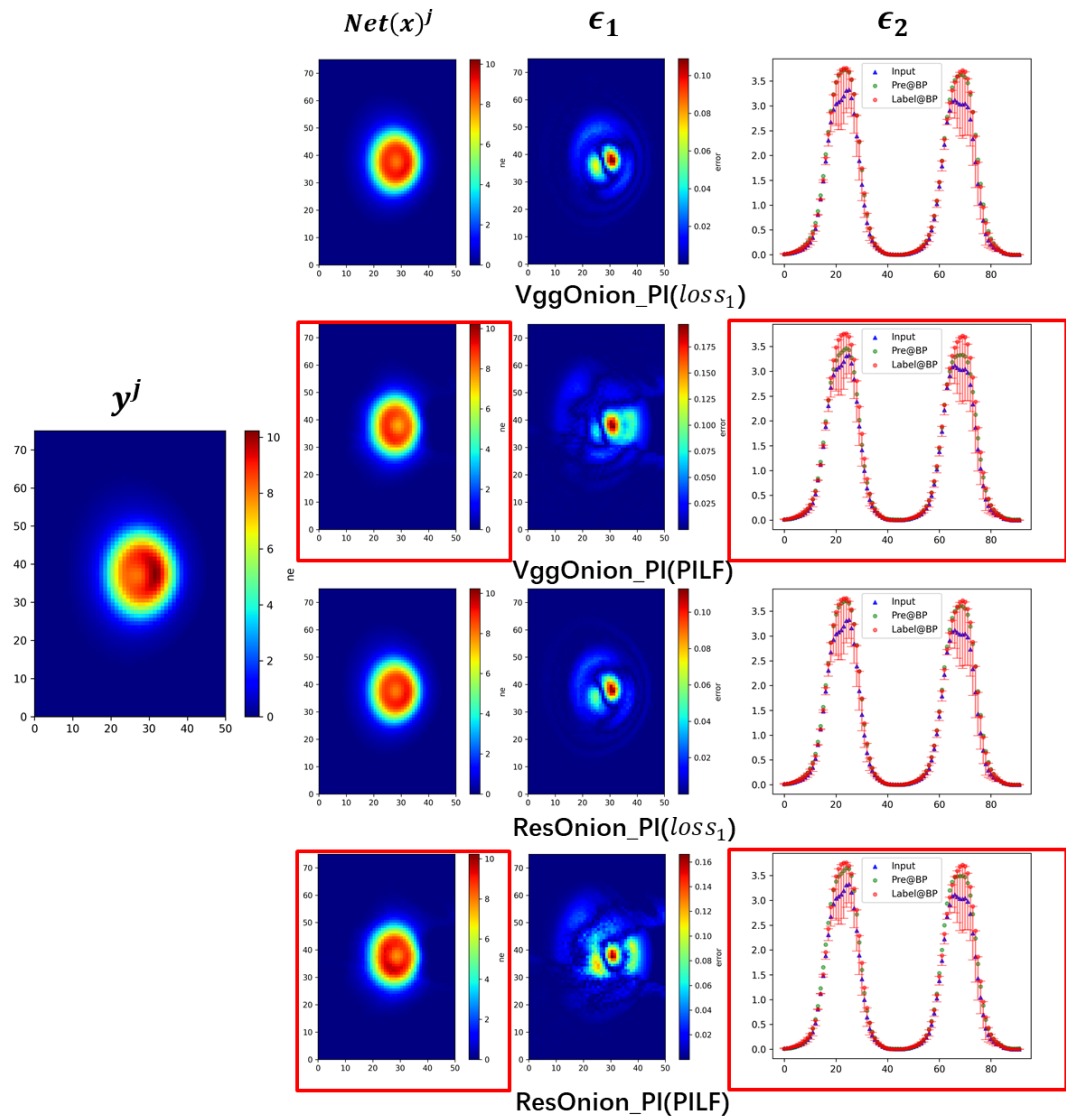


Figure 11 Test results of different models on the j th sample in the EXP_East test set.

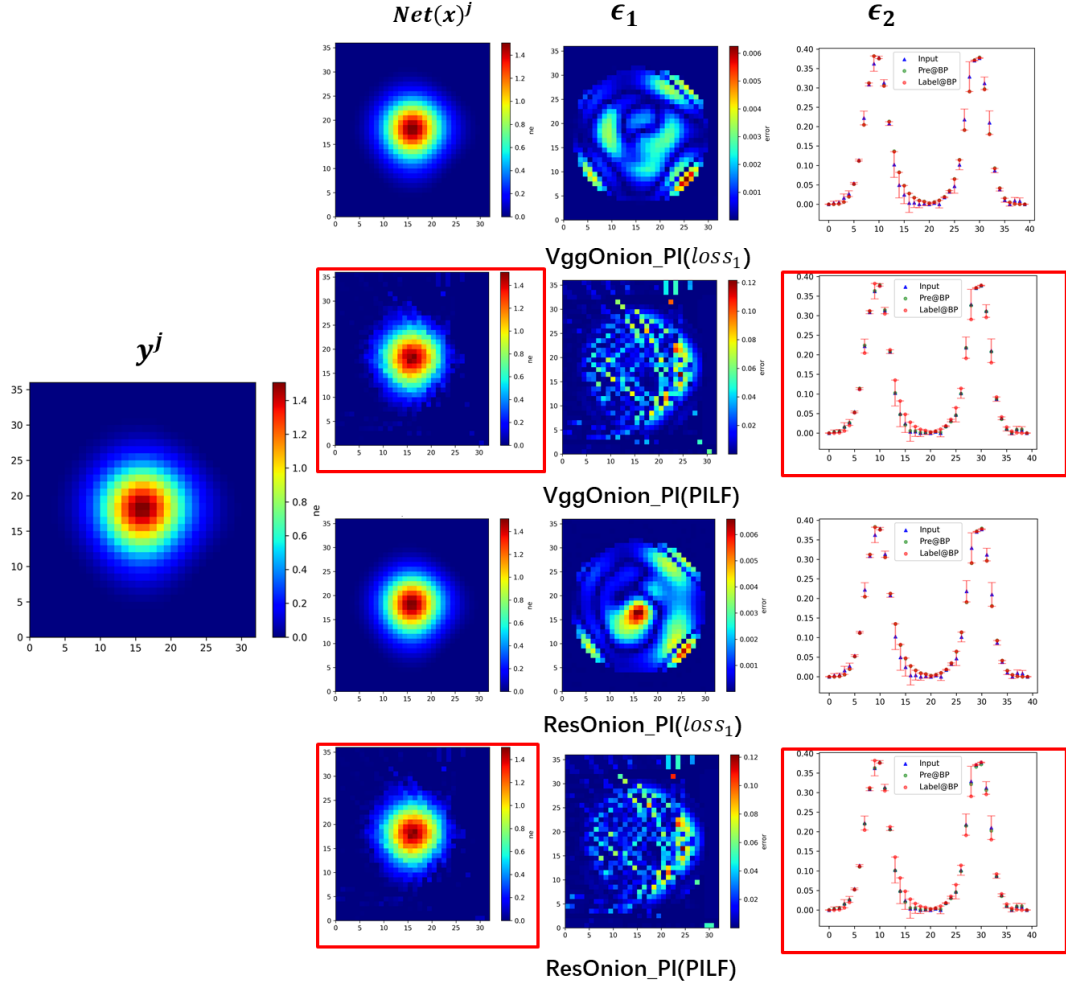


Figure 12 Test results of different models on the j th sample in the EXP_HL-2A test set.

6 Conclusion

In this paper, we constructed four models based on the proposed Physics-Informed Deep Learning Model Architecture and conducted experimental analyses using four distinct datasets. Initially, we theoretically discussed the most rational approach to incorporating Physical Information (PI) and empirically validated this theory. The introduction of PI enhanced model performance to varying degrees across different datasets. Subsequently, to address issues at the edges of the results, we further employed the Softplus activation function, which, due to its characteristics aligning with the properties of the physical quantities in question, significantly improved the edges of the prediction results. It was also observed that the Softplus activation function substantially boosted model performance. Finally, we compared and analyzed the impact of the Physics-Informed loss function (PILF). The adoption of PILF effectively constrained the predictions, ensuring they better satisfied the inherent physical constraints. The hyperparameter c_1 must be adjusted according to the specific context. The model demonstrates satisfactory performance across datasets from different devices.

Incorporating updated backbone networks, an expanded dataset, and higher-quality data will likely lead to further enhancements in model performance. In the future, the AUX diagnostic dataset from ENN Science and Technology Development Co., Ltd. will be made

available in the code repository. The experiment data during the current study are not publicly available for legal/ethical reasons but are available from the corresponding author on reasonable request.

Acknowledgments

The authors express their sincere gratitude to Dr. Liqing Xu and Dr. Chaowei Mai from the Hefei Institute of Plasma Physics, Chinese Academy of Sciences, for their invaluable assistance and support throughout this research. Special thanks are also extended to Dr. Dong Li from the Southwest Institute of Physics, China National Nuclear Corporation, and to Dr. Xianli Huang and Cong Zhang from the ENN Science and Technology Development Co., Ltd. for their contributions and encouragement. Their expertise and guidance have been instrumental to the success of this work. This work is supported by the National Natural Science Foundation of China (No. 12405266).

Reference

1. Seo, J. *et al.* Development of an operation trajectory design algorithm for control of multiple 0D parameters using deep reinforcement learning in KSTAR. *Nucl. Fusion* **62**, 086049 (2022).
2. Seo, J. *et al.* Multimodal Prediction of Tearing Instabilities in a Tokamak. in *2023 International Joint Conference on Neural Networks (IJCNN)* 1–8 (IEEE, Gold Coast, Australia, 2023). doi:10.1109/IJCNN54540.2023.10191359.
3. Vega, J. *et al.* Disruption prediction with artificial intelligence techniques in tokamak plasmas. *Nat. Phys.* **18**, 741–750 (2022).
4. Fu, Y. *et al.* Machine learning control for disruption and tearing mode avoidance. *Physics of Plasmas* **27**, 022501 (2020).
5. Kates-Harbeck, J., Svyatkovskiy, A. & Tang, W. Predicting disruptive instabilities in controlled fusion plasmas through deep learning. *Nature* **568**, 526–531 (2019).
6. Degraeve, J. *et al.* Magnetic control of tokamak plasmas through deep reinforcement learning. *Nature* **602**, 414–419 (2022).

7. Seo, J. *et al.* Avoiding fusion plasma tearing instability with deep reinforcement learning. *Nature* **626**, 746–751 (2024).
8. De Vries, P. C. *et al.* Survey of disruption causes at JET. *Nucl. Fusion* **51**, 053018 (2011).
9. Ferreira, D. R. Applications of Deep Learning to Nuclear Fusion Research. Preprint at <http://arxiv.org/abs/1811.00333> (2018).
10. Blatzheim, M., Böckenhoff, D., & the Wendelstein 7-X Team. Neural network regression approaches to reconstruct properties of magnetic configuration from Wendelstein 7-X modeled heat load patterns. *Nucl. Fusion* **59**, 126029 (2019).
11. Matos, F., Svensson, J., Pavone, A., Odstrčil, T. & Jenko, F. Deep learning for Gaussian process soft x-ray tomography model selection in the ASDEX Upgrade tokamak. *Review of Scientific Instruments* **91**, 103501 (2020).
12. Simonyan, K. & Zisserman, A. Very Deep Convolutional Networks for Large-Scale Image Recognition. Preprint at <http://arxiv.org/abs/1409.1556> (2015).
13. Mai, C. *et al.* Application of deep learning to soft x-ray tomography at EAST. *Plasma Phys. Control. Fusion* **64**, 115009 (2022).
14. Wang, Z. *et al.* Deep Learning Based Surrogate Model a fast Soft X-ray (SXR) Tomography on HL-2 a Tokamak. *J Fusion Energ* **43**, 52 (2024).
15. Dosovitskiy, A. *et al.* An Image is Worth 16x16 Words: Transformers for Image Recognition at Scale. Preprint at <http://arxiv.org/abs/2010.11929> (2021).
16. Liu, Z. *et al.* Swin Transformer: Hierarchical Vision Transformer using Shifted Windows. Preprint at <http://arxiv.org/abs/2103.14030> (2021).

17. Liu, Z. *et al.* KAN: Kolmogorov-Arnold Networks. Preprint at <http://arxiv.org/abs/2404.19756> (2024).
18. Beck, M. *et al.* xLSTM: Extended Long Short-Term Memory. Preprint at <http://arxiv.org/abs/2405.04517> (2024).
19. Wang, C. *et al.* Gold-YOLO: Efficient Object Detector via Gather-and-Distribute Mechanism. Preprint at <http://arxiv.org/abs/2309.11331> (2023).
20. Xu, W. & Wan, Y. ELA: Efficient Local Attention for Deep Convolutional Neural Networks. Preprint at <http://arxiv.org/abs/2403.01123> (2024).
21. Xia, C., Wang, X., Lv, F., Hao, X. & Shi, Y. ViT-CoMer: Vision Transformer with Convolutional Multi-scale Feature Interaction for Dense Predictions. Preprint at <http://arxiv.org/abs/2403.07392> (2024).
22. Vaswani, A. *et al.* Attention Is All You Need. Preprint at <http://arxiv.org/abs/1706.03762> (2023).
23. Li, D. *et al.* Bayesian tomography and integrated data analysis in fusion diagnostics. *Rev. Sci. Instrum.* **87**, 11E319 (2016).
24. Wu, T. *et al.* Compositional Generative Inverse Design. Preprint at <http://arxiv.org/abs/2401.13171> (2024).
25. He, K., Zhang, X., Ren, S. & Sun, J. Deep Residual Learning for Image Recognition. Preprint at <http://arxiv.org/abs/1512.03385> (2015).